First results from the ground calibration of the NuSTAR flight optics

Jason E. Koglin[a*], HongJun An[a], Nicolas Barrière[b], Nicolai F. Brejnholt[c], Finn E. Christensen[c], William W. Craig[b], Charles J. Hailey[a], Anders Clemen Jakobsen[c], Kristin K. Madsen[d], Kaya Mori[a], Melania Nynka[a], Monica Fernandez-Perea[e], Michael J. Pivovaroff[e], Andrew Ptak[f], Clio Sleator[a], Doug Thornhill[a], Julia K. Vogel[e], Daniel R. Wik[f], William W. Zhang[f]

[a]Columbia Astrophysics Laboratory, New York, NY
[b]University of California, Berkeley, CA
[c]Danish Technical University, Copenhagen, Denmark
[d]California Institute of Technology, Pasadena, CA
[e]Lawrence Livermore National Laboratory, Livermore, CA
[f]Goddard Space Flight Center, Greenbelt, MD

ABSTRACT

NuSTAR is a hard X-ray satellite experiment to be launched in 2012. Two optics with 10.15 m focal length focus X-rays with energies between 5 and 80 keV onto CdZnTe detectors located at the end of a deployable mast. The FM1 and FM2 flight optics were built at the same time based on the same design and with very similar components, and thus the performance of both is expected to be very similar. We provide an overview of calibration data that is being used to build an optics response model for each optic and describe initial results for energies above 10 keV from the ground calibration of the flight optics. From a preliminary analysis of the data, our current best determination of the overall HPD of both the FM1 and FM2 flight optics is 52", and nearly independent of energy. The statistical error is negligible, and a preliminary estimate of the systematic error is of order 4". The as-measured effective area and HPD meet the top-level NuSTAR mission sensitivity requirements.

Keywords: Hard X-ray telescope, X-ray optics, segmented glass, NuSTAR

1. THE NUSTAR MISSION

The Nuclear Spectroscopic Telescope Array (NuSTAR) is a NASA Small Explorer (SMEX) satellite mission that will open the hard X-ray frontier (5-80 keV) to sensitive exploration.[1] NuSTAR builds on the High Energy Focusing Telescope (HEFT) balloon program, using a simple design with extensive heritage.[2] The focusing optics described here together with pixelized CdZnTe detectors will make NuSTAR ~100 times more sensitive than previous experiments. All scientific instruments have been delivered and integration with the spacecraft is well under way in preparations for a February 2012 launch. A Pegasus launch to a 6° inclination, low-earth (550-600 km) orbit provides a stable, low-background environment. NuSTAR will soon be the first telescope to provide true imaging capability in the hard X-ray band, a natural place to study black holes, neutron stars and other extreme physical environments.

The NuSTAR instrument consists of two co-aligned conical-approximation Wolter-I optics that focus onto Cadmium Zinc Telluride (CdZnTe) detector arrays shielded by Pb/CsI scintillators. The optics and detectors are separated by a 10 m mast that extends after launch with a laser metrology system to monitor the mast alignment. The CdZnTe detectors provide excellent spectral resolution and high quantum efficiency without requiring cryogenic operation (see T. Kitaguchi et al., "Spectral calibration and modeling of the NuSTAR CdZnTe pixel detectors", SPIE 8145-7).[3] The optics utilize thin glass shells coated with depth-graded multi-layers to extend the bandpass over that achievable with standard metal surfaces and provides high performance over the 12' x 12' detector field of view (FOV). The overall calibration of the NuSTAR effective area (including optics, focal plane detectors and windows/covers) relies on a combination of ground calibration measurements of the individual instruments and in-flight measurements of the system as a whole. Here we describe initial results from the ground calibration of the NuSTAR flight optics.

* Correspondence: koglin@astro.columbia.edu, http://www.astro.columbia.edu/~koglin

Optics for EUV, X-Ray, and Gamma-Ray Astronomy V, edited by Stephen L. O'Dell, Giovanni Pareschi,
Proc. of SPIE Vol. 8147, 81470J · © 2011 SPIE · CCC code: 0277-786X/11/$18 · doi: 10.1117/12.895279

2. OPTICS DESIGN AND FABRICATION

The NuSTAR optics design has been described elsewhere,[4,5] and the fabrication of the NuSTAR flight optics is described in detail in these proceedings (Craig et al., "Fabrication of the NuSTAR Flight Optics", SPIE 8147-15, 2011).[6] Here we briefly summarize the aspects of the optics design and fabrication that are of particular importance to calibration of the effective area and point spread response function (PSF). The NuSTAR optics are composed of 133 concentric layers of conical-approximation Wolter I mirrors aligned and held together by epoxy and precisely machined graphite spacers that run along the optic axis. Each layer is composed of an upper and a lower set of segmented mirrors, 0.21 mm thick and 225 mm long. The innermost (outermost) layer has a radius of 54.4 mm (191.2 mm) and a conic graze angle of 1.3 mrad (4.7 mrad). The inner 68 layers are composed of 6 × ~60° sectors (sextants) and the outer 65 layers are composed of 12 × ~30° sectors (dodecant). The NuSTAR glass substrates are created by thermally slumping 210 μm thick glass microsheets onto polished forming mandrels.[7,8] At least 10% of the mirrors are also measured with the interferometer at GSFC immediately after forming for quality assurance and feedback into the forming process.

Table 1: Summary of components for the two NuSTAR Flight Optics Modules.

266	Wolter-I Optic Shells
4752	Mounted Mirrors
24,048	Graphite Spacers
48,096	Epoxy Bondlines
10	Baseline Multilayer Formulas
243	Multilayer Coating Runs (each with a witness sample)
82.7	m^2 of Mirror Surface Area
1.4 Million	Layers of Multilayer Coatings

Depth-graded multilayers are applied to the optical surfaces in a production coating facility at the Danish Technical University (DTU) that uses planar magnetron sputtering. A multilayer structure is a stack of thin layers of alternating materials designed so that the small reflections from each layer add in phase. Depth-graded multilayers vary the bi-layer thickness so that different layers are optimized to reflect different wavelengths, providing broadband response. The specific multilayer design depends on graze angle, which scales with the optic radius. The 133 shells are divided into 10 groups optimized for a particular range of graze angles. Before coating, the substrates are cleaned using a three step ultrasonic process and sorted by radius for application of the appropriate design. Quality is assured for each coating run by including a silicon wafer as a witness that is characterized immediately at 8 keV and subsequently over the full energy range. These reflectance data, as well as housekeeping data from the coating chamber are automatically logged to the optics database, also updated to reflect the coating applied to each substrate. The material combinations for the coatings depend on graze angle – the inner 7 radius groups (about 2/3 of the geometric area) are coated with Pt/C, and the remaining are coated with W/Si. Details of the multilayer coating are described in these proceedings (Christensen et al., "NuSTAR flight coatings: what did we really do", SPIE 8147-29, 2011).[9]

After multilayer coating, the figure of each mirror is measured with the laser scanner at Columbia before mounting.[10] The coated substrates are assembled into an optic using two assembly machines at Columbia University's Nevis Laboratory. The assembly machines, which were built by ABtech[†], comprise precision air-bearing axes mounted on solid granite bases and provide exceptional machining tolerances. The machines are housed in a class 1000 clean room with temperature and humidity control, and the air-bearings machine components require no oils that could potentially contaminate the optics. Our error-compensating, monolithic assembly and alignment (EMAAL) procedure involves constraining each mirror segment with five machined graphite spacers that run along the optical axis, which are precisely machined to the correct radius and angle. In this process, the nominally cylindrical glass segments are forced to a conical form, and in the process, radial mismatches are removed. The inner three sets of upper/lower spacers are

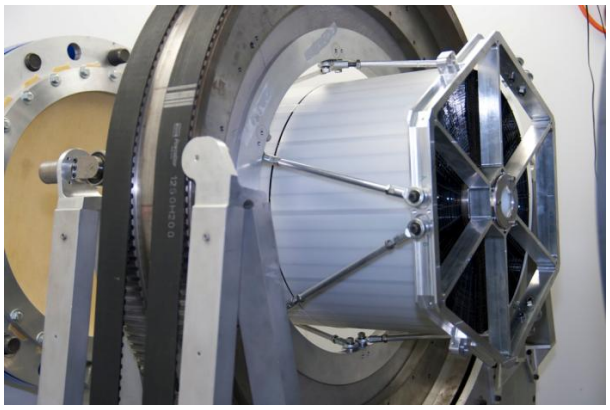

Figure 1: NuSTAR optic pictured in calibration room mounted in the calibration bench.

[†] http://www.abtechmfg.com

individually mounted with 'single-shoe strongback' fixtures while each outmost spacer is mounted together with the outermost spacer from the adjacent mirror segment using a 'double-shoe strongback'. Concentric layers of glass are stacked on top of each other starting with a central mandrel and building outward. The radius and angle of each layer of spacers is machined with respect to the optical axis (not the last layer) such that there is never any stack-up error during fabrication. The transition from sextant to dodecant mirrors is made with three intermediate sextant layers using nine spacers per sector with wide outside spacers that are shared by adjacent mirrors to provide azimuthal connectivity of the three transition layers. After construction, support spiders were attached to the inner mandrel, and an alignment cube was also bonded to each end of the optic to serve as a permanent reference surfaces throughout calibration and integration.

An important advantage to our mounting method is that metrology is performed in-situ as the optic is being assembled. An air-bearing Linear Variable Differential Transformer (LVDT) built by CPPI[‡] is used to perform low force surface metrology on the back surface of the mounted mirrors.[11,12] Since the thickness of mirror substrates is very uniform in the axial direction, surface metrology performed on the back-side of the glass replicates the front surface figure which serves to focus the X-rays. Complete surface figure maps of each mirror shell are obtained from LVDT data recorded along the entire axial length of both upper and lower shells at 144 different azimuth positions. The LVDT device itself is linear over a 100 um range with an accuracy of 0.5%. The LVDT resolution is dominated by noise introduced in the scanning process. We sample the output voltage from the Lion Amplifier (±10 V signal) at a rate of 250 Hz using LabVIEW and a National Instruments multifunction DAQ (NI612). A low pass filter is applied to the data to remove noise introduced in the data acquisition process. The data is filtered using a 5th order Butterworth and a length scale of 5 mm. The filtered data is then differentiated to determine the slope errors of the mirror surface. The HPD performance is calculated for each mirror, and the surface height/slope profiles can be used as input in raytrace models.

3. OPTICS GROUND CALIBRATION

An optic with focal length focusing X-rays from an infinite source distance is illustrated in the Figure 3a cartoon. Since a large-aperture and parallel source of X-rays is not available on the ground, it is not possible to directly measure the optics response before launch. Further, each optic is composed of thousands of mirrors each with over a hundred layers of multilayer materials that have a complex reflectivity response to graze angle and energy (see Table 1 for a summary of the optics components). The ground calibration of past hard X-ray optics for balloon missions has been conducted at existing synchrotron and long-beam facilities.[13,14,15] Here we describe the ground calibration approach for the NuSTAR optics for which a dedicated calibration facility was used.

3.1 Optics Response Model (ORM)

The ground calibration involves building up an Optics Response Model (ORM) based on a raytrace simulation using measured data from the optics components and/or witness samples before and during fabrication. The ORM is first calibrated using a set of detained measurements from an X-ray source at a finite distance, and then validated through independent and complementary X-ray measurements including:

- Detailed measurements of spectral response of Flight Optics measured for the complete optic and groups of mirrors with a high purity Germanium (Ge) detector as well as silicon drift detector (SDD) for the low energy response.
- Measurements of PSF as a function of energy using one-dimensional slit scans of the optic masked to limited azimuthal extent.
- Fine measurements of the PSF of complete optics measured with high resolution (0.1 mm) X-ray imager.

3.2 X-ray Calibration Measurements at the Rainwater Memorial Calibration Facility (RaMCaF)

The Rainwater Memorial Calibration Facility (RaMCaF) is a 163 m long hard X-ray calibration facility,[16] which is conveniently located right next to the assembly room for the NuSTAR optics at Columbia's Nevis Laboratory. The Comet MXR-160 X-ray tube with tungsten target supplies the facility with X-rays up to 100 keV (see Figure 2 for the source spectrum). An overview of its use for the NuSTAR flight optics calibration is presented in these proceedings (Brejnholt et al., "NuSTAR ground calibration: The Rainwater Memorial Calibration Facility (RaMCaF)", SPIE 8147-

[‡] http://www.coloradoprecision.com/LVDT2.htm

16, 2011).[17] It describes the facility setup for the NuSTAR flight optics and an overview of the types of calibration measurements that were performed. It also illustrates the optics alignment procedure and modeling of small mounting distortions that occurred during the ground calibration which are important to second order when evaluating the ground calibration data, but will not be present in space.

The X-ray ground calibration measurements for the FM1 and FM2 flight optics, including installation and alignment, were performed over a period of 18 consecutive days (March 5-22, 2011). A series of three basic types of measurements are made to calibrate and verify the ORM.

1. Full flood illumination of the entire optic.
2. Full flood illumination of an entire figure of revolution, but restricting the radial extent of illumination to a group of mirrors coated with the same multilayer formula.
3. Measurements of a portion of the optic restricted in both azimuthal and radial extent such that the effective beam divergence from the X-ray source is much less than the optics PSF and can to first order be neglected.

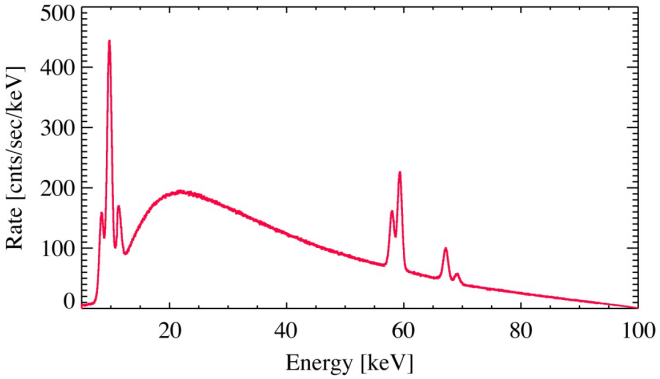

Figure 2: Measured X-ray Source Spectrum.

Generally speaking, the measurements of the limited portion of the optic are used to calibrate the ORM, and the full illumination measurements are used to validate the ORM. Figure 3b illustrates an optic of focal length F being fully illuminated by an X-ray source at a finite distance S. The effective focal distance for a finite source distance follows the lens equation: $1/F' = 1/S - 1/F$. The graze angle of a conic approximation shell of radius R is given by $\alpha = R/(4F)$, and $\gamma = R/S$ is the source divergence angle at the same shell at a radius R. The ratio $\gamma/\alpha = 4F/S$ is approximately the fraction of the optic that is not illuminated during full-flood illumination. In this way, to good approximation the Wolter-I optic acts as a thin lens. Due to the conic approximation design, there is no fundamental aberration in the image for either off-axis or finite source distance measurements (as long as one accounts for the change in effective focal distance).

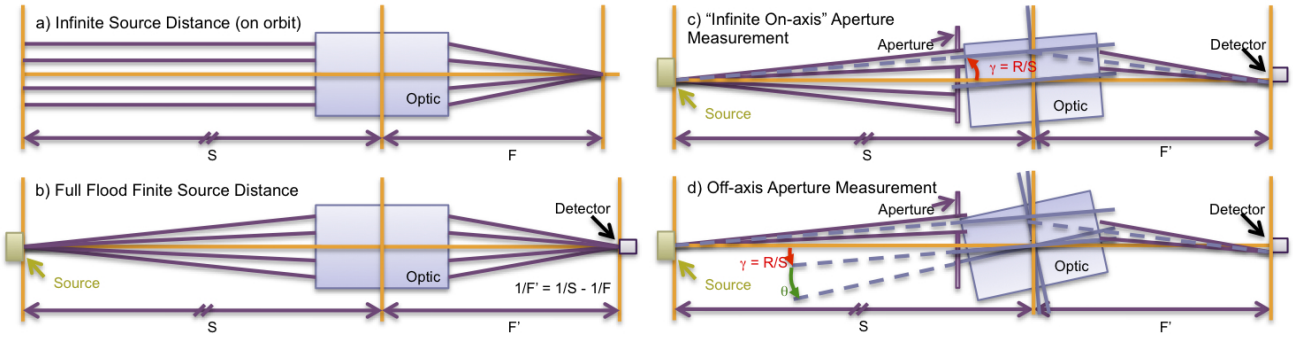

Figure 3: **a)** The upper left cartoon shows an optic with focal length F focusing X-rays from an infinite source distance. **b)** The lower left cartoon shows the case for an X-ray source at a finite distance S. The effective focal distance for a finite source distance follows the lens equation: $1/F' = 1/S - 1/F$. **c)** The upper right cartoon depicts the beam aperture restricted to illuminate only a limited number of shells with nominal radius R and a limited azimuthal extent and rotating the optic by an angle $\gamma = R/S$ so that that group of shells is effectively points directly at the source as illustrated in the top cartoon (view from above). **d)** Off-axis angles for a limited aperture can be measured by rotating the optic an additional amount θ as illustrated in the lower left cartoon.

To very good approximation we can measure the on-axis optics response by restricting the beam aperture on the optic to a limited number of shells with nominal radius R and a limited azimuthal extent and rotating the optic by an angle $\gamma = R/S$ so that that group of shells is effectively pointed directly at the source as illustrated in Figure 3c (view from above). The radial group apertures limit the exposure to 6-8 mirror layers and together with the azimuth extent of 60 degrees. The rms beam divergence over the aperture opening from the source at 163 m is limited to 3" to 10" for the inner to outer radial groups, respectively; and the finite source size (~5 mm) contributes an additional ~5" to the beam divergence. The

optic is rolled about its axis to position the other sectors in the aperture opening and performing similar measurements. The response of limited portions of the optic to off-axis angles can be measured by rotating the optic an additional amount θ. Here we are illustrating only 'yaw' rotations in the horizontal plane, and in practice both the pitch and yaw of the optic must be moved in coordination as a function of optic roll to truly measure the response of a complete optic at a single off-axis angle. Given limited calibration time available, we instead chose to make a systematic set of measurements to use to calibrate an optics response model as will be described in Section 6.

4. OPTICS RESPONSE MODEL INPUT DATA

The following section provides an overview of the measurements used as input into the optics response model (ORM).

4.1 Surface Metrology for Length Scales above ~1 mm

The following summarizes the measurements directly on each mirror before and after mounting to determine the surface figure on length scales above ~1 mm.

- ~3000 Interferometer Measurements of Glass Substrates (~15% of mirrors, ~>1 mm length scale)
- >200,000 Axial Laser Surface Profiles (>25% before coating and 100% after coating, >1 mm length scale)
- 114,912 Axial LVDT Surface Profiles (>5 mm length scale)

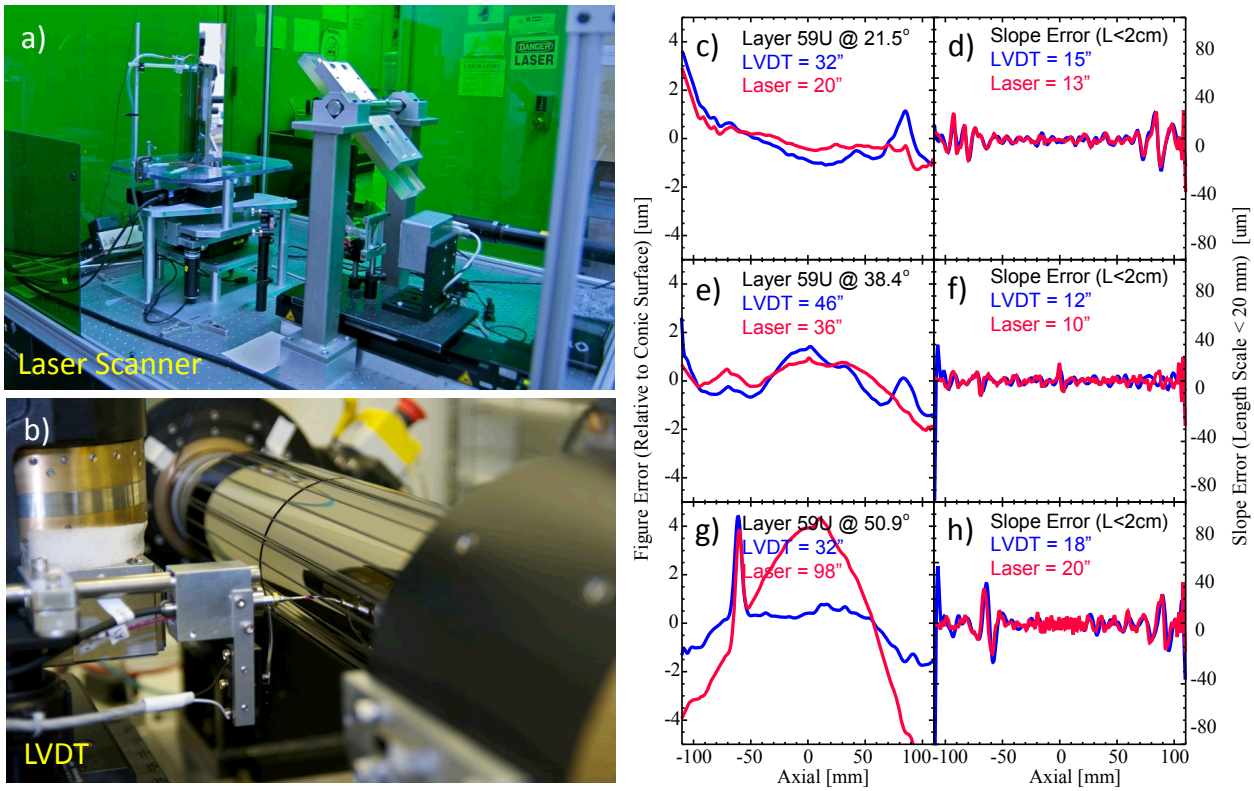

Figure 4: **a)** The Laser scanner at Columbia University used to measure the surface figure of every flight mirror before mounting is show in the upper left. **b)** The LVDT metrology system, which is used to measure each layer in-situ as the optic is being fabricated, is shown in the lower left. **c) e) g)** A comparison of the LVDT and laser data for three axial scans is shown in a series of plots to the right.. In the left column, the surface height relative to a perfect conic surface is plotted versus axial position at three azimuthal positions on the upper layer 59 shell for LVDT and laser data in blue and red, respectively. **d) f) h)** In the right column, the slope errors on length scales less than 2 cm are similarly plotted versus axial position for LVDT and laser data.

As previously described the surface figure is measured for each mirror prior to mounting with a laser scanner (see Figure 4a) and immediately after it is mounted with an LVDT (see Figure 4b). The interferometer measurements were used primarily as an early independent verification of the analysis and processing of the laser data in addition to serving as

immediate feedback into the mirror forming process. Axial scan data for the LVDT and laser scanner are compared at nine example azimuthal positions in Figure 4 and Figure 5. In the left columns, the surface height relative to a perfect conic surface is plotted versus axial position at three azimuthal positions for LVDT and laser data in blue and red, respectively. In the right columns, the slope errors on length scales less than 2 cm are plotted versus axial position for LVDT and laser data (again in blue and red, respectively).

Overall, the intrinsic cylindrical figure error of the glass substrates (before potential introduction of deformations due to multilayer coating stress) and the mounting process provide about the same overall figure error contribution which is typically quantified in terms of the half-power-diameter (HPD), the diameter within which half the power/energy is focused. The mounting process with the five spacer configuration is very successful in transforming the cylindrical mirrors to the correct conic angle and radius, typically with less than a few arcsecond overall slope error. The mounting process also highly suppresses the large scale bows in the mirrors that can occasionally be substantial (>10 μm) near the azimuthal edges due to stress that is sometimes introduced in the multilayer coating (e.g., see laser/LVDT comparison in Figure 4g and Figure 5k). The mounting process does typically introduce some figure error on the 20-50 mm length scale, generally through imperfect machining of spacers, alignment/conformance errors in the application of the graphite spacers with 'strongback' mounting hardware (e.g. Figure 5g), or interference of the spacer constraint with sharp features in the glass surface (thought to originate from dust contamination between the glass and forming mandrel during slumping). On length scales less than ~2 cm the mirrors generally contribute only 10-20" to the HPD, and the intrinsic figure of the mirror on this length scale is rarely affected by the mounting process as is clearly evident by the excellent correlation between laser and LVDT slope data in the right columns of the plots. A series of three consecutive axial scans in the plots to the left of Figure 5 illustrate the potential to mount mirrors at the 20" level.

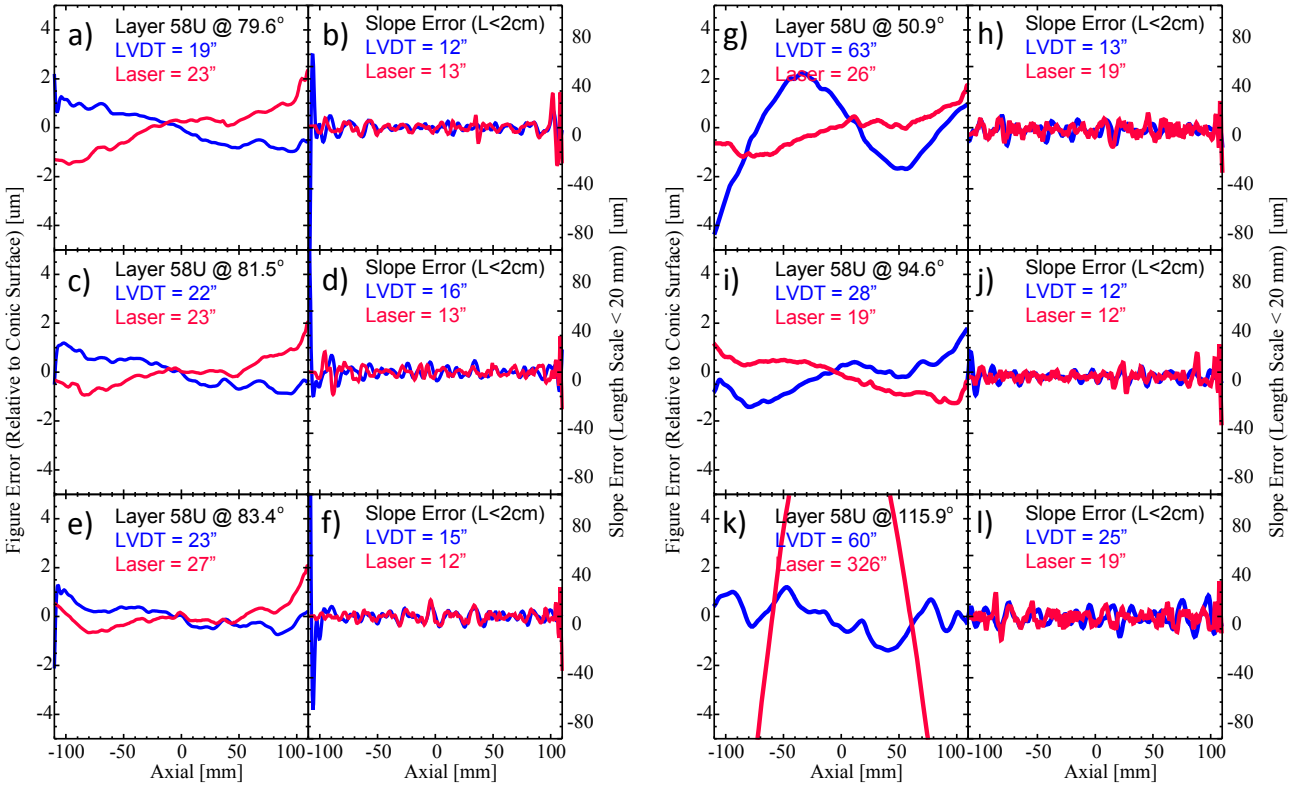

Figure 5: Three axial LVDT and Laser scans are compared in the series of plots to the left and right for layer 58 upper shells (see Figure 4 for description).

4.2 Measurements of Mirror Surfaces and Multilayer Coatings on nm to mm Length Scales

The following summarizes the measurements to mechanically characterize the flight mirrors and multilayer coatings over nm to mm length scales:

- 20 Atomic Force Microscopy (AFM, Digital Instruments Dimension 5000™) Images (coated & uncoated)

- ~12 Optical Profilometry (Zygo NewView™) Images (Coated & uncoated)
- 6 Transmission Electron Microscopy (TEM) of Multilayer Witness Samples and Flight Coatings (>100 Images)

The power spectral density (PSD) has been computed for both W/Si and Pt/C coated flight mirrors based on atomic force microscopy (AFM) and Zygo white light interferometry studies of the surface of flight-spare mirrors. The PSD for each is plotted versus spatial frequency in Figure 6. The two-dimensional PSDs span six orders of magnitude in length scale and are well-described a power-law model. The high-spatial frequency roughness (see caption for more details) is 0.29 nm rms for the Pt/C coating and 0.30 nm rms for the W/Si coating. This low level of surface roughness suggests that we should see minimal contributions to the PSF from scattering, compared to low-spatial frequency or figure errors.

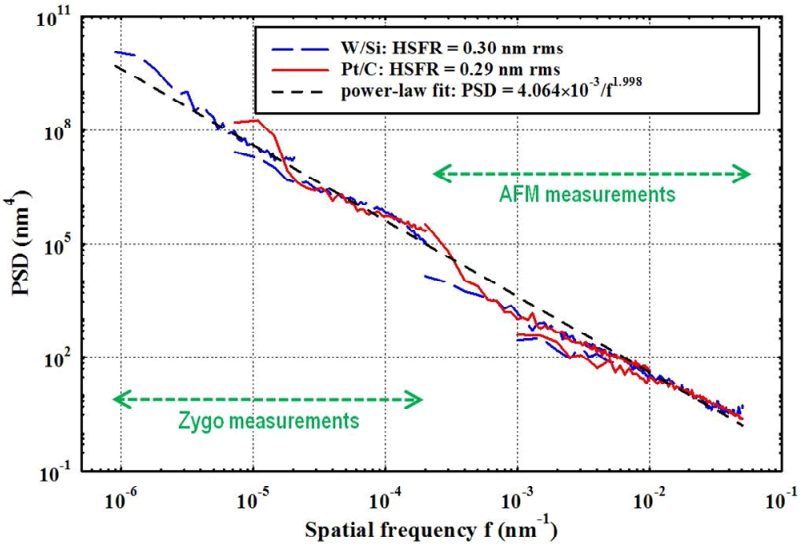

Figure 6: The two-dimensional power spectral density (PSD) computed from AFM and Zygo studies is plotted versus spatial frequency for two NuSTAR flight-spare mirrors. The dashed blue and solid red lines are for NuSTAR flight mirrors with W/Si and Pt/C multilayer coatings, respectively. The PSD is obtained by computing the 2D Fourier transform of the surface maps. The rms roughness σ is calculated by evaluating the expression $\boldsymbol{\sigma^2 = \int_{f_1}^{f_2} 2\pi f\, S(f)\, df}$, where $S(f)$ is the PSD, f is the spatial frequency, $f_1 = 5\times10^{-4}$ nm^{-1} and $f_2 = 5\times10^{-2}$ nm^{-1}.

As previously mentioned, the LVDT data is filtered on a length scale of 5 mm. Thus, any surface features on length scales less than 5 mm will not be observed. The laser scanner directly measures surface slope features and probes length scales down to the length scale characterized by the laser spot size of ~1 mm. From a comparison of the laser and LVDT data on very short length scales, we deduce that length scales from 1-5 mm contribute <1-3" to the HPD.

A series of Transmission Electron Microscopy (TEM) images of increasing magnification was performed for a number of multilayer coated witness samples and flight mirrors. From this we measure the thicknesses for each bilayer throughout the multilayer stack. This is valuable in developing a multilayer parameterization to model the d-spacing progression in order to limit the number of free parameters when fitting the multilayer response using X-ray measurements.

4.3 Spectral Response of Multilayer Coatings (6-95 keV)

The following summarizes the spectral response measurements of multilayer coatings over the 6-95 keV energy range:

- 306 Multilayer Coating Uniformity Measurements at 8 keV (covering all coating geometries)
- 243 Multilayer Witness Sample Measurements at 8 keV
- ~25 Flight Mirror Measurements at 8 keV
- 10 High energy X-ray scatter measurements at a synchrotron facility (planned)
- >500 Multilayer Witness Sample Spectra (6-95 keV); ~2 angles/sample (>350 completed)
- 13 Flight Mirror Spectra (6-95 keV)

The multilayer response measurements are described elsewhere in these proceedings (see Christensen et al., "NuSTAR flight coatings: what did we really do", SPIE 8147-29, 2011).[9]

5. POINT SPREAD RESPONSE FUNCTION (PSF) MEASSUREMENTS

Below is a summary of the NuSTAR Flight Optic X-ray Measurements conducted at RaMCaF:

- 2 High-resolution Image Composites of the FM1 and FM2 optics (entire FOV including 'Ghost-rays')
- 90 High-resolution Images Composites vs. Pitch/Yaw and Beam/Aperture Configuration (~1000 total images)
- 27 Detailed PSF Scans for FM1/2 (1539 total spectra)
- 32 PSF Scans with 2 deg Aperture for FM2 Inner Mirrors (800 total spectra)
- 32 PSF Scans with 2 deg Aperture for FM2 Outer Mirrors (800 total spectra)

5.1 High Resolution Imaging of the PSF

A focal plane image of the fully-illuminated FM2 optic is shown in Figure 7. It was obtained using an X-ray camera developed by RMD Inc.[§] that uses a CsI(Tl) scintillator coupled to an electron multiplying CCD (EMCCD).[18] For reference, the 12x12' FOV of the CdZnTe detector focal plane is shown. With 0.1 mm resolution, one clearly sees the spacer and spider obscuration in the 'Ghost-rays' (i.e., X-rays that only intersect the upper mirror surface), which extend beyond the CdZnTe FOV. A similar focal plane image of the FM1 optic but where an aperture plate that provides exposure to only four of the 20 radial groups is shown to the right. Each ring is comprised of single-bounce 'ghost-rays' from radial groups of 6-8 mirror shells. For a more detailed discussion of these images see Vogel et al.[19]

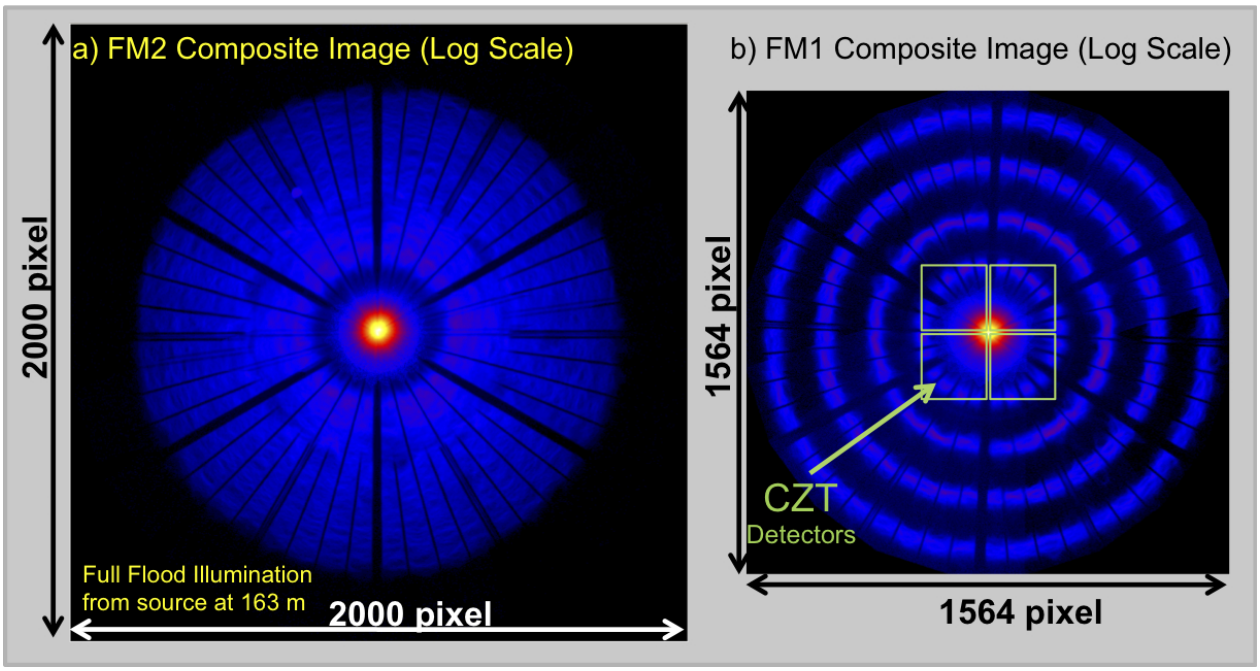

Figure 7: a) Composite focal plane image (0.1 mm pixel size) for the FM2 optic fully illuminated by a broadband source at a distance of 163 m plotted with log scale intensity. **b)** A similar focal plane image of the FM1 optic but where an aperture plate that provides exposure to only four of the 20 radial groups is plotted with the same pixel size. Distict rings are visible from the single bounce X-ray rings for radial subgroups 1, 9, 15 and 19. The size of the CdZnTe detectors shown for scale.

5.2 One-dimensional profile measurements of the PSF for each 60 degree sector

PSF measurements were performed with the non-imaging Ge and SDD detectors by scanning slits in the detector focal plane. Given time constraints it was not practical to make 2-dimensional scans. Instead, 1D PSF profiles were obtained by masking a 60 degree opening about a sextant sector on the horizontal axis and scanning the detector slits in the horizontal detector plane. Given that the sector has an azimuthal aperture exposure of 60 degrees centered about the

[§] http://www.rmdinc.com/

horizontal plane, and the PSF due to azimuthal figure errors is suppressed by the ratio of the radius to focal length (i.e., ~10x), the PSF to first approximation lies only in the horizontal plane.

To more closely approximate the case of an infinite source, the optic was rotated in yaw so that the central radius of that sector pointed to the X-ray source such that the inner/outer shell is effectively +/- 1.5' off-axis. The optic was successively rolled by 60 degrees and profile measurements repeated on the complete optic. The normalized PSF of each sector is plotted in six energy bands in Figure 8 and Figure 9 for the FM1 and FM2 optics, respectively. The bins for X > 20 mm become dominated by single bounce X-rays from the upper shells (i.e., 'ghost-rays'). Since the relative area of single-bounce X-rays to that of the primary core goes inversely with energy (i.e., with reflectivity for one bounce and reflectivity squared for two-bounce), one expects the single bounce X-ray flux from high energy X-rays to be relatively higher than at low energy where the reflectivity approaches unity.

To calculate the HPD, each profile was fit with a four parameter King Distribution, $A[1+(x-x_o)^2/r_o^2]^{-\alpha}$, where A is the overall normalization factor and r_o and α parameterize the shape of the PSF such that decreasing values of α provide increasing energy in the wings. The offset in the peak position x_o is currently left as a free parameter given that there is a residual wobble when rolling the optic from sector to sector. Further, a slight temporary asymmetry in the PSF is present for the ground calibration measurements due to gravitational sag (~1 mdeg) and the alignment struts introducing a parabolic bend in the optic mandrel (~2 mdeg) that acts over all of the mirror layers.[17] The fit range of -25 < X < 15 mm was used to avoid contamination of single bounce X-rays. The HPD was calculated from the fit parameters for an infinite focal plane.

The overall HPD is measured to be 52" and independent of X-ray energy for both the FM1 and FM2 optics. The small dependence on the HPD versus sector is thought to be due to the bend induced by the calibration bench mount fixturing. Any gravitational distortion will be nearly identical for the six measurements due to azimuthal symmetry and is less important given the sector measurements are performed in the horizontal plane.

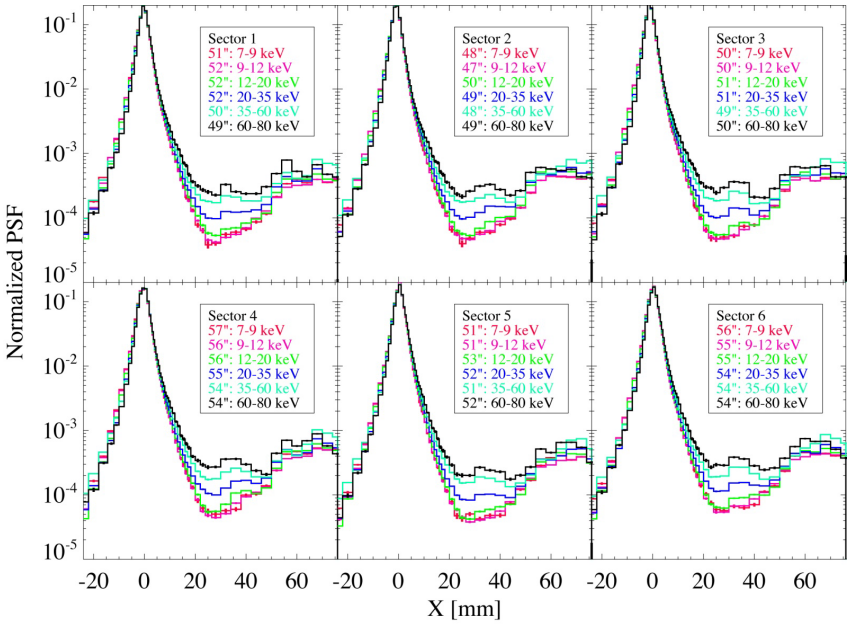

Figure 8: The normalized PSF of each 60 degree sector of FM1 is plotted in six energy bands.

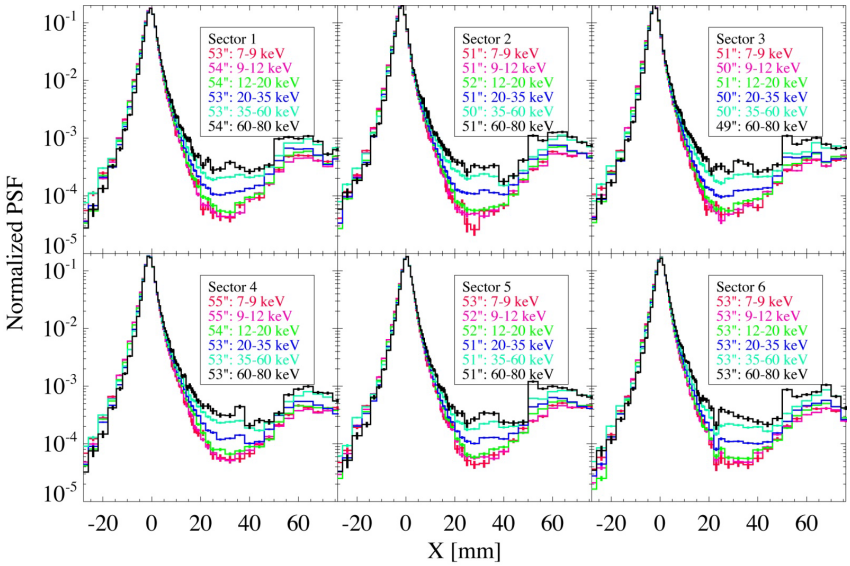

Figure 9: The normalized PSF of each 60 degree sector of FM2 is plotted in six energy bands.

The systematic error associated with this analysis is estimated to be of order 4" and likely dominated by this bend distortion with additional systematics associated with detector slit calibration, finite X-ray source size/distance, finite aperture effects and fitting procedure. Gravitational effects will not be present on orbit, and the optics were installed and mechanically aligned in the spacecraft with the optical axes aligned vertically (i.e., along the gravity vector) with a technique to avoid introducing stress on the optics.[6] Detailed raytrace simulations are required to fully quantify the systematic error and potentially introduce small corrections.

5.3 Azimuthal dependence of the PSF for Sector 1

The azimuthal dependence of the PSF was also measured in 2 degree steps over Sector 1 with a 2 degree azimuthal aperture. In this case the outer layers composed of dodecant (30°) mirror segments were masked off to focus on making a series of 1D PSF scans of the sextant (60°) mirrors in steps of 2 degrees as illustrated in Figure 10a. The process repeated with the sextant mirrors masked as illustrated in Figure 10b. The HPD measured in six energy bands is plotted as a function of azimuth position for the inner and outer mirrors in Figure 10c and Figure 10d, respectively. A first order approximation to the HPD based on LVDT data is also plotted.

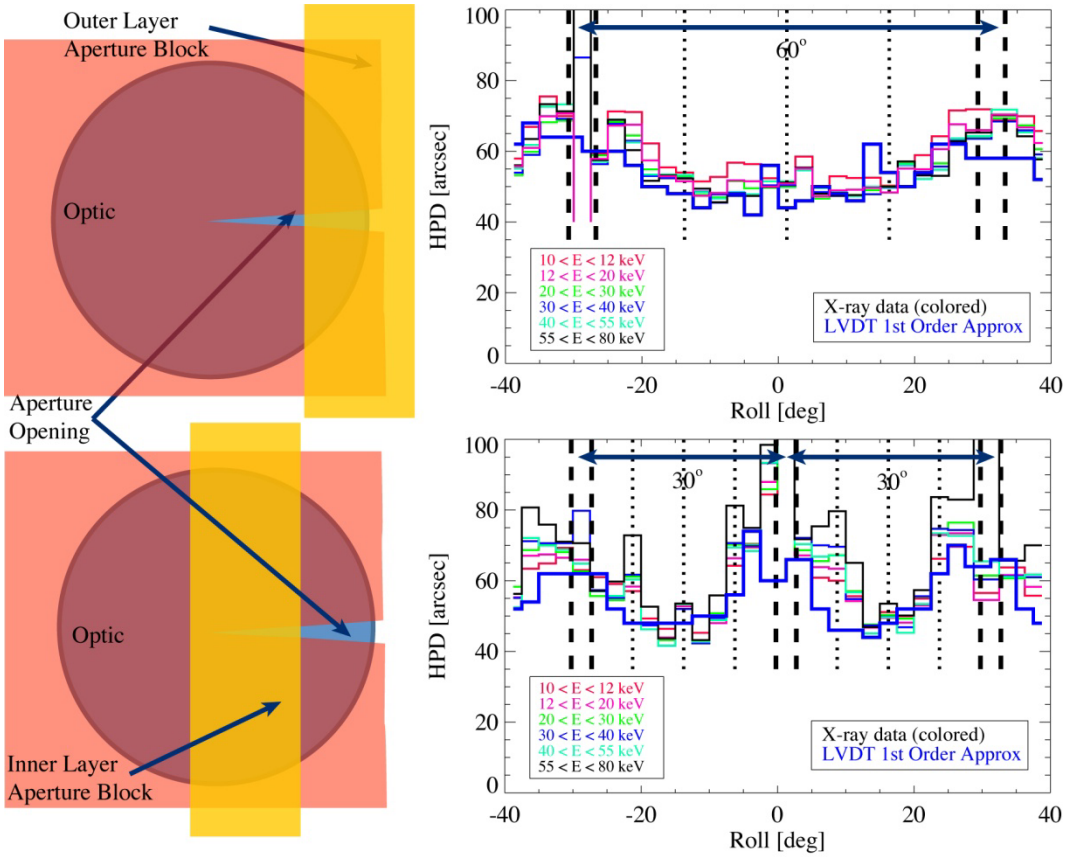

Figure 10: The HPD measured in six energy bands is plotted as a function of azimuth position. A first order approximation to the HPD based on LVDT data is also plotted.

There is a trend of poorer performance toward the outer portions of the mirrors that was apparent during assembly based on the LVDT data. This is largely attributed to the challenge in consistently using the 'double-shoe strongback' hardware where each outmost spacer is mounted together with the outermost spacer from the adjacent mirror segment so that both spacers are completely within the 7 mm wide spider mount structure (as previously described in Section 2). Thus, while the 'double-shoe' design helped to maximize the overall throughput of the optic, it also likely contributed to a slight degradation in the overall PSF performance. It is also possible that some of this is due to residual stress in the multilayer coating which causes an increasing axial bow with azimuthal position from the mirror center. Generally, there is little energy dependence in the measured HPD except at higher energies for the dodecant mirrors where the reflectivity becomes very low and any impact to the overall HPD would be minimal.

6. EFFECTIVE AREA MEASUREMENTS

6.1 Data Analysis Approach

The measurement of $I_o(E)$ (the direct X-ray beam measurement without optic) and I(E) (the X-ray beam passed through the response of the optic) are performed using a Germanium (Ge) spectrometer. In each case the response of the detector must be taken into account to appropriate normalize the I(E) measurements. For an X-ray source or radioactive source with lines sufficiently narrow that the effective area $A_{eff}(E)$ is constant over the linewidth, a simple ratio (with at most a small correction) of I/I_o yields the effective area. We have developed an algorithm for correcting the off-diagonal response of the Ge spectrometer so that the effective area can be directly determined over a broad energy range through the simple normalized beam ratio $A_{eff} = I/I_o$. This is possible because a detailed GEANT4 response model of the Ge detector we used has been carefully cross-calibrated with a well calibrated spare detector from RHESSI[20]. In this way, a detailed source model is not required, and when properly implemented results in only a slight additional smoothing of the intrinsic ~1 keV energy resolution of the Ge detector. The main requirement is that each spectrum, including the direct beam normalization, is well calibrated in energy and corrected for rate effects (e.g., deadtime and pileup). The linearity of the Ge detector together with the Amptek DP5 digital pulse processor we used is observed to be constant with time; however, we observed ~1 keV shifts in the zero energy offset of the DP5 spectra with both rate and time. The zero energy offset of every spectrum is automatically calibrated based using the position of the seven Tungsten emission lines that are present in the X-ray source spectrum (see Figure 2). Deadtime and pileup are discussed in Section 6.4.

We are also developing a forward fitting procedure. In this approach, a parametric model of the source spectrum $I_o(E_\gamma)$ must be developed based on the measured source data $M_o(h_\gamma) = I_o(E_\gamma)\ R(E_\gamma,h_\gamma)$ using the detector response matrix $R(E_\gamma,h_\gamma)$ where h_γ is the measured pulse height of an input X-ray with energy E_γ. The optic/sample response $A_{eff}(E_\gamma)$ can then be fit based on the measured spectrum, $M(h_\gamma) = A_{eff}(E_\gamma)\ I_o(E_\gamma)\ R(E_\gamma,h_\gamma)$.

For the energy region below ~15 keV, a Silicon detector, with excellent energy resolution, augments the baseline Ge spectrometer measurements. We are currently still developing the X-ray source model and detector response functions for the Silicon based detectors. Thus, we restrict our discussion of initial calibration results to the I/I_o effective area analysis from the Ge detector.

A Silicon 'beam monitor' detector was in place continuously to record absolute intensity and spectral shape of the beam. The Comet X-ray source is intrinsically very stable and repeatable and the beam vacuum and environmental conditions (e.g., temperature, atmospheric pressure and humidity) were relatively stable over the entire flight calibration period; thus, only modest corrections of the source spectrum below ~10 keV are required. Periodic measurements of the direct beam with the Ge and SDD detectors, together with the Si beam monitor and environmental monitoring throughout the RaMCaF facility, allow us to accurately model variations in the low-energy source flux versus time. However, since a complete processing and modeling of this data is not yet completed, we report only on results above 10 keV where the maximum variations in vacuum pressure and environmental conditions are inconsequential to the direct beam normalization. In this way we use the average direct beam spectrum that was measured throughout the calibration period to normalize all of the data.

Since energies below 10 keV do not penetrate deeply, the response is effectively described by total external reflection from the top high density multilayer material (Pt or W) modified by the topmost low density material (~25 μm of C or Si). Surface contamination would also alter the response below 10 keV; however, measurements multilayer and glass samples at 8 keV show no signs of surface contamination[9], and the epoxy used for manufacturing the optics was selected that has a low level of outgassing with contribute negligibly to scatter and absorption.[21]

6.2 Flight Optic X-ray Measurement Summary

Below is a summary of the NuSTAR Flight Optic X-ray Measurements conducted at RaMCaF:

- 150 Full-flood Illumination Pitch/Yaw Scans for FM1/2 (3505 total spectra)
- 62 Yaw/Pitch Scans of 60 deg Sectors for FM1/2 (1252 total spectra)
- >600 Coarse Scans of the PSF Core (7 scan spectra plus a 'check-sum' spectra each, >4000 total spectra)
- >2000 Multilayer Spectra from Single Bounce X-rays from the Upper Mirror Shells
- >100 Additional Custom/Specialty Scans

- >1000 Direct Beam and Background Spectra
- >2000 Beam Uniformity Spectra
- >50,000 Total Spectra (including setup, alignment and slit calibration)

6.3 Multilayer Spectra from Single Bounce X-rays from the Upper Mirror Shells

Coarse scans with 2 mm wide slits were performed over the single-bounce X-ray peak for each radial group at four angles for Sector 1 and one angle for the other five sectors. The single bounce spectra for SG8, Sector 1 are plotted in Figure 11 for scans for successively larger effective graze angles. Within each plot, five spectra are shown for the measurements with significant statistics, each of which samples a 19" portion of the PSF. In this, way, we directly measure the average multilayer response of the six mirrors in SG8 at 15 relatively discrete angles and over the full energy range. From these spectra, one clearly sees the effect of the initial drop in reflectivity move to lower energy as the graze angle becomes larger in going from the left to right plots. Similarly, the energy at which the reflectivity begins to cut off due to the wavelength becoming smaller than the smallest bilayer shifts to lower energy with increasing graze angle. While the reflectivity will be difficult to normalize absolutely from these spectra, they provide the relative response of bulk response of the mirrors including variations in each coating run, variations in uniformity across the mirror surface as well as ~1 Å higher roughness than in the silicon witness samples. These SG8 measurements are for a set of 6 mirrors from 4 different coating runs, each of which is slightly different including one where the power in the cathode dropped out for a period of time, thus altering the response. The nominal angles in the left and right most plots roughly correspond to the witness sample angles that we standardly measure. Thus we can compare this data with the expected response based on the measured witness sample response corrected for increased mirror roughness and the coating uniformity that has been mapped out for each coating geometry.

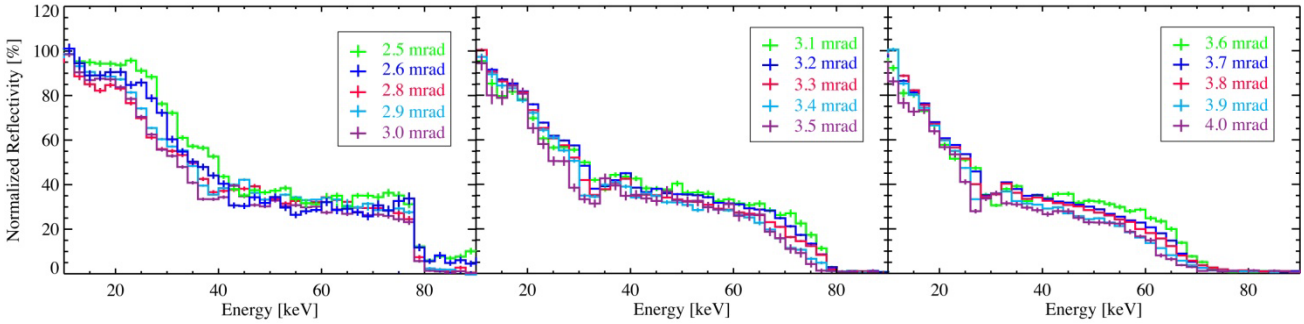

Figure 11: The single bounce spectra for SG8, Sector 1 are plotted for scans at three yaw angles such that the nominal graze angle for of the single bounce X-rays are 2.8, 3.3 and 3.8 mrad for the plots from left to right. Within each plot, 4-5 spectra are shown for the measurements with significant statistics, each of which samples a 19" portion of the PSF.

6.4 Coarse PSF Scans as a Check on the Dead-time and Pileup Model

Coarse PSF scans consisting of seven variable width steps sample horizontal image profile over a full width of 20 mm. The detector slit widths range from 1.5 to 5 mm with a constant slit height of 12 mm. These 20 second coarse scan measurements are followed by a single 40 second measurement at a lower beam current with slits open to the full width of 20 mm. The wide slit "check-sum" measurement provides a cross-check of the sum of the seven sample measurements (i.e., "scan-sum") to assure that the detector dead-time and pile-up is correctly modeled. As an example, the measured spectra, pileup model and measured background are plotted in Figure 12a for both the "scan-sum" and "check-sum" measurements. The event rates vary substantially over the seven scan measurements (that comprise the scan-sum spectra) and check-sum measurements and thus each has significantly different pileup and deadtime correction factors. Between the Pt cutoff and 100 keV where the reflectivity is very low, the measured spectra become dominated by pileup events and above 100 keV there are no source X-rays. Figure 12b shows the "check-sum and "scan-sum" spectra normalized to the direct beam spectra after pileup and deadtime correction as well as an off-diagonal detector response correction. This comparison demonstrates that detector deadtime and pileup are well understood over a very broad input count range.

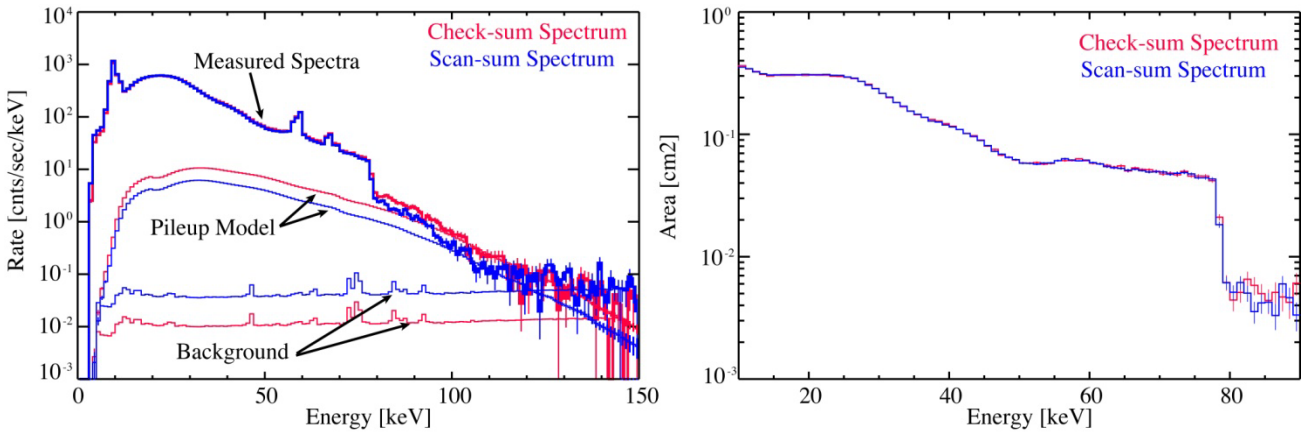

Figure 12: The measured spectra, pileup model and measured background (each indicated in the plot with arrows) are plotted above for the sum of the seven coarse PSF yaw spectra (i.e., 'Scan-sum') in blue and the single measurement with 20 mm wide slits (i.e., 'Check-sum') in red. The lower plot shows the check-sum and scan-sum spectra normalized to the direct beam spectra after pileup and deadtime correction as well as an off-diagonal detector response correction. This comparison demonstrates that detector deadtime and pileup are well understood over a very broad input count range.

6.5 Effective Area of Radial Groups Measured Through Coarse PSF Scans

Coarse PSF scans were performed at nine off-axis angles for Sector 1 of each of the 20 radial subgroups using Ge and/or SDD detectors. Additionally, all of the other five sectors were measured near on-axis. The angles at which measurements were performed for FM2 are plotted in Figure 13. As an example, the normalized counts in six energy bands are plotted versus the seven horizontal slit positions in Figure 14a and the corresponding normalized reflectivity for each position is plotted in Figure 14b along with the checksum spectra for wide (+-10 mm) slits. The spectra in the 2-bounce have less features than the multilayer witness samples or the single bounce spectra since they are a convolution of graze angles from the upper and lower mirror surfaces.

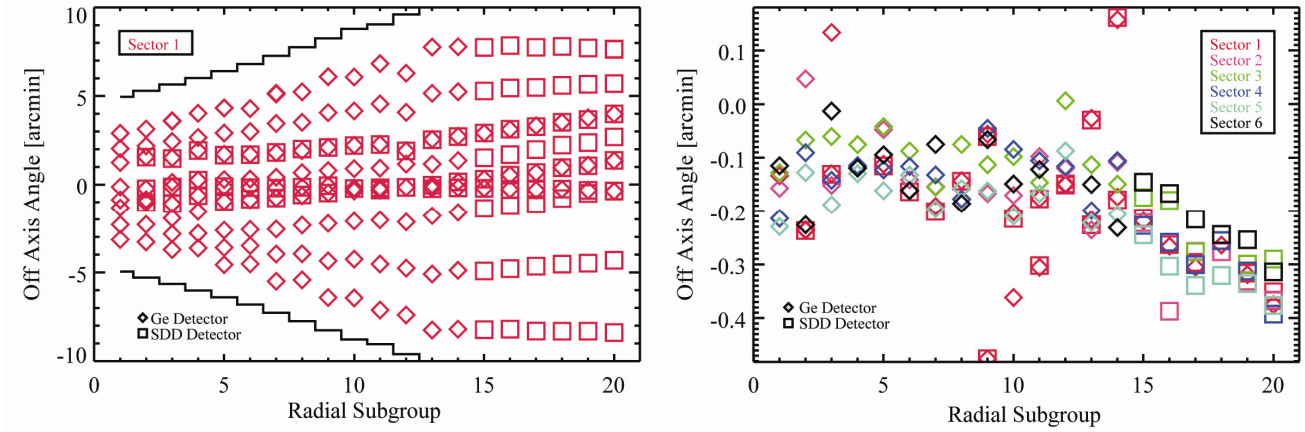

Figure 13: **a)** The effective off-axis angle of each coarse scan of the FM2 PSF core for Sector 1 is plotted versus radial subgroup. Diamonds and rectangles denote measurements for the Ge and SDD detectors, respectively. **b)** The coarse PSF scan 'near on-axis' angle for every FM2 sector is plotted versus radial subgroup.

The coarse PSF scan spectra for SG8, Sector 1 and a simplified response model are compared at nine yaw angles in the plots in Figure 15. The yaw angle of the optic with respect to the equivalent on-axis angle of an infinite source for this radial subgroup is noted for each of the nine spectra. The model contains a simplified PSF and multilayer response. The overall throughput in the model is fixed based on the prior design assumption that epoxy at each of the spacer positions causes 1.0 mm of obscuration in addition to the 1.2 mm spacer width together with each spider structure obscuring 7 mm (covering the outermost spacers of each mirror).

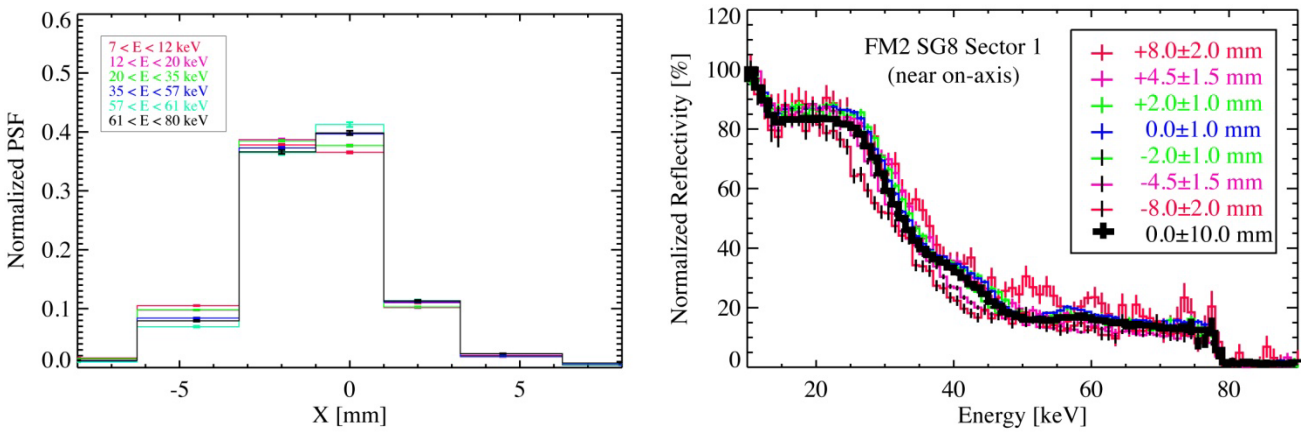

Figure 14: The normalized counts in six energy bands are plotted to the left versus the seven horizontal slit positions for an example coarse scan over the 2-bounce PSF core (SG8, Sector1, near infinite on-axis). The normalized reflectivity in each band is plotted to the right for each of the seven positions along with the checksum spectra for wide (±10 mm) slits. The spectra in the 2-bounce have less features than the multilayer witness samples or the single bounce spectra since they are a convolution of graze angles from the upper and lower mirror surfaces.

The collective response is well characterized to first order even in a simplistic model. We expect that the finer multilayer response will be modeled much better after including the measured coating uniformity appropriate for each individual mirror, and we expect that the increased measured throughput at the extreme angles will be better understood with a full modeling of the mirror figure based on the LVDT surface metrology data.

The absolute effective area determined through coarse PSF measurements for each of the 20 radial subgroups is plotted above as a function of energy in Figure 16. For each case the optic was rotated in yaw to the appropriate angle to approximate on-axis response to a source at infinity. These spectra are summed in Figure 17 to provide a model independent measurement of the on-axis effective area. Since these measurements are only approximately on-axis, an optics response model is required to make modest corrections to build the true on-axis response. However, since the optics response is maximum on-axis, this will generally result in an increase in effective area particularly towards the higher energies where the effective area drops off more rapidly with off-axis angle. A complete calibration of the optics response model using the 9 off-axis angles for each radial subgroup will provide a calibrated off-axis response for the NuSTAR optics.

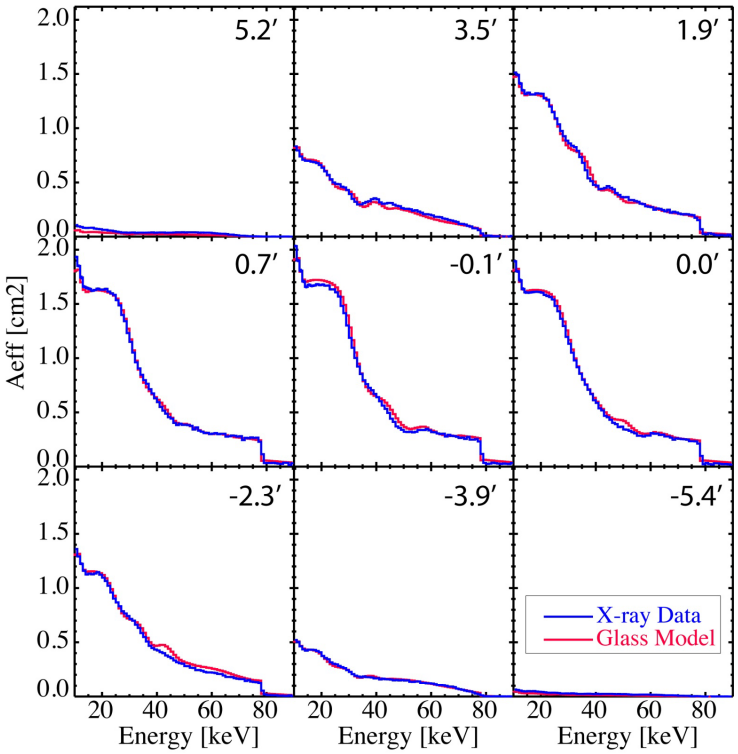

Figure 15: The spectra of SG8, Sector 1 at nine yaw angles are plotted along with a simplified response model. The yaw angle of the optic with respect to the equivalent on-axis angle of an infinite source for this radial subgroup is noted for each of the nine spectra.

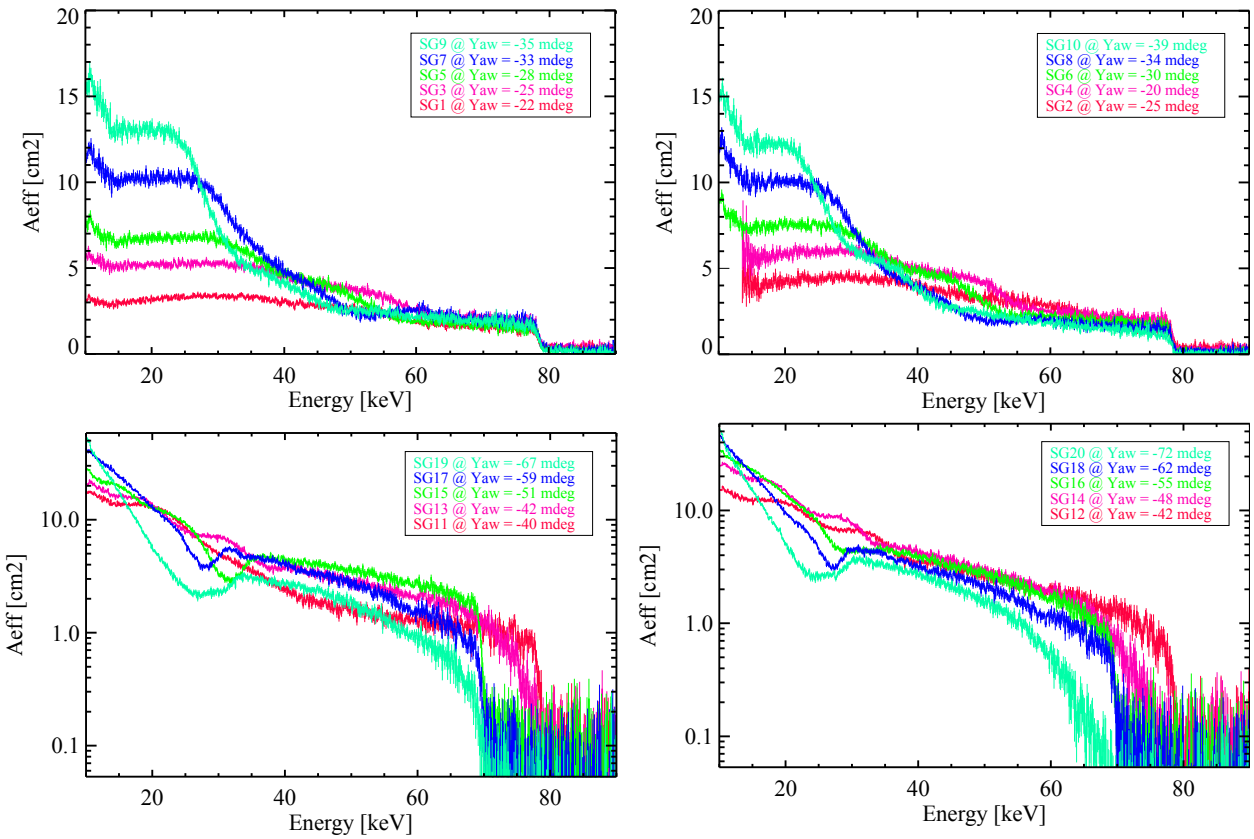

Figure 16: The absolute effective area for each of the 20 radial subgroups is plotted above as a function of energy. For each case the optic was rotated in yaw to the appropriate angle to approximate on-axis response to a source at infinity.

While we have concentrated on data for FM2 in this paper, both optics were calibrated in succession over a period of just over two weeks, and a similar set of data was acquired for FM1. In this way, we have sufficient data to independently calibrate each optic. The FM1 and FM2 were built at the same time with very similar component parts including the same multilayer coating design. While some of the mirrors for FM1 and FM2 were coated in the same coating runs (particularly for layers 1-30), a majority of the mirrors for the two optics were coated in separate coating runs (although with the same coating designs). Thus, the optics response models for the two optics will be quite similar, with the differences serving as systematic checks of the component data that is used as input.

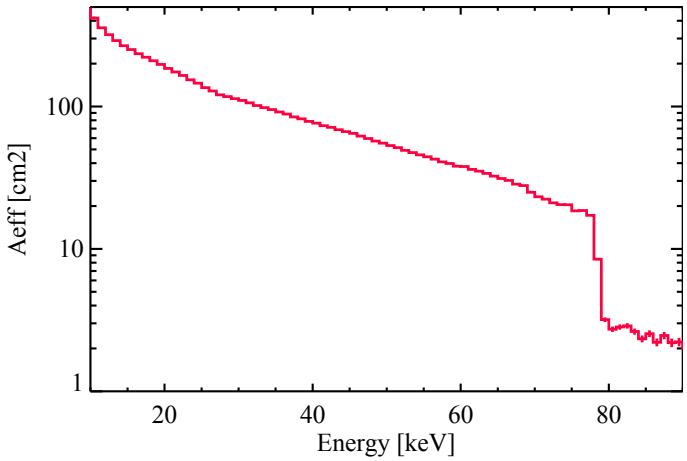

Figure 17: The combined effective area of the combined radial group measurements near on-axis are plotted versus energy.

7. CONCLUSIONS

From a preliminary analysis of the data, our current best determination of the overall HPD of both the FM1 and FM2 flight optics is 52", and nearly independent of energy. The statistical error is negligible, and a preliminary estimate of the systematic error is of order 4". The as-measured effective area and HPD meet the top-level NuSTAR mission sensitivity requirements. While these are preliminary results, they are not expected to change significantly as we continue to develop a complete optics response model both the FM1 and FM2 optics.

We gratefully acknowledge the technical support Zeshan Haier provided in setting up and maintaining the RaMCaF calibration facility for the FM1 and FM2 measurements. This work is supported by a NASA contract to Columbia University, NNG08FD60C, "The Nuclear Spectroscopy Telescope Array (NuSTAR): Bringing the High Energy Universe into Focus." Part of this work was funded by the Technical University of Denmark (DTU Space). Part of this work was also performed under the auspices of the U.S. Department of Energy by Lawrence Livermore National Laboratory under Contract DE-AC52-07NA27344. LLNL contributions included support from LDRD project 10-SI-007. The use of the RMD X-ray detector for optics calibration was made possible thanks to NASA SBIR Grant NNX11CH32P. The prototype SDD development is funded by IRAP, the French National Center for Scientific Research (CNRS) and the Centre National d'Etudes Spatiales (CNES).

REFERENCES

[1] Harrison, F.A. et al., "The nuclear spectroscopic telescope array (NuSTAR)," Proc. SPIE 7732-27 (2010).

[2] Harrison, F.A. et al., "HEFT and NuSTAR focusing telescopes," Experimental Astronomy, Volume 20, Issue 1-3 (2005) 131-137.

[3] Kitaguchi, T. et al., "Spectral calibration and modeling of the NuSTAR CdZnTe pixel detectors," Proc. SPIE 8145-7 (2011).

[4] Koglin, J.E. et al., "NuSTAR Hard X-ray Optics Design and Performance," Proc, SPIE 7437(2009).

[5] Hailey, C.J. et al., "The Nuclear Spectroscopic Telescope Array (NuSTAR): Optics Overview and Current Status," Proc. SPIE 7732-28 (2010)

[6] Craig, W.W. et al., Fabrication of the NuSTAR Flight Optics," Proc. SPIE 8147-15 (2011)

[7] Zhang, W.W. et al., "Manufacture of mirror substrates for the NuSTAR missionm" Proc. SPIE 7437-20 (2009).

[8] Zhang, W.W. et al., "Fabrication of glass mirror segments for the International X-ray Observatory," Proc. SPIE 7732-51 (2010).

[9] Christensen, F.E. et al., "NuSTAR flight coatings: what did we really do," Proc. SPIE 8147-29 (2011).

[10] Koglin, J.E. et al., "NuSTAR Hard X-ray Optics," Proc. SPIE 5900-33 (2005).

[11] Koglin, J.E. et al., "Development and Production of Hard X-ray Multilayer Optics for HEFT," Proc. SPIE 4851, 607-618 (2003).

[12] Koglin, J.E. et al., "Production and Calibration of the first HEFT Hard X-ray Optics module," Proc. SPIE 5168, 100-111 (2004).

[13] Gubarev, M. et al., "Alignment, Assembly and Testing of High-Energy X-ray Optics," Proc. SPIE 5900 (2005).

[14] Koglin, J.E. et al., "Calibration of HEFT Hard X-ray Optics," Proceedings of the X-ray Universe 2005, 955 (2006).

[15] Ogasaka, Y. et al., "Characterization of a Hard X-ray Telescope at Synchrotron Facility SPring-8," Japanese Journal of Applied Physics, Vol. 47, No. 7, pp. 5743-5754 (2008).

[16] Brejnholt, N.F. et al., "The Rainwater Memorial Calibration Facility (RaMCaF) for X-ray optics," X-ray Optics and Instrumentation, Article in press (2011).

[17] Brejnholt, N.F. et al., "NuSTAR ground calibration: The Rainwater Memorial Calibration Facility (RaMCaF)," Proc. SPIE 8147-16 (2011).

[18] Thacker, S. C. et al., "Development of a high-speed CT imaging system using an EMCCD Camera," Proc. SPIE 7258-46 (2009).

[19] Vogel, J. K. et al., "Application of an EMCCD Camera for Calibration of Hard X-ray Telescopes," IEEE Proceedings, Article in preparation (2011).

[20] Lin, R.P. et al., "The Reuven Ramaty High-Energy Solar Spectroscopic Imager (RHESSI) mission," Proc. SPIE 5171, 38-52 (2004).

[21] An, H. et al., "Evaluation of epoxy for use in NuSTAR optics," Proc. SPIE 7437 (2009).